Tuning of Thermometric Performances of Mixed Eu–Tb Metal–Organic Frameworks through Single-Crystal Coordinating Solvent Exchange Reactions

Andreas Kourtellaris, William Lafargue-Dit-Hauret, Florian Massuyeau, Camille Latouche, Anastasios Tasiopoulos, Hélène Serier-Brault

ADVANCED OPTICAL MATERIALS
www.advopticalmat.de

Tuning of Thermometric Performances of Mixed Eu–Tb Metal–Organic Frameworks through Single-Crystal Coordinating Solvent Exchange Reactions

Andreas Kourtellaris, William Lafargue-Dit-Hauret, Florian Massuyeau, Camille Latouche, Anastasios J. Tasiopoulos,* and Hélène Serier-Brault**

An initial investigation on the employment of targeted structural alterations, achieved through the post-synthesis modification method, for modulation of the thermometric properties of metal–organic frameworks (MOFs) is reported. The MOF $Eu_{0.05}Tb_{0.95}$-NBDC (NBDC = 2-amino-1,4-benzenedicarboxylate) is chosen as pristine material, and its terminal *N*,*N*-dimethylformamide (DMF) molecules are exchanged by various terminal and chelating ligands through a single-crystal-to-single-crystal coordinating solvent exchange reaction. Temperature-dependence luminescence studies reveal that all samples are highly sensitive in the medium range with a maximum relative sensitivity of 2.6% K^{-1} at 190 K for $Eu_{0.05}Tb_{0.95}$-NBDC. In addition, a shift of 50 K of the operating temperature range is evidenced for the exchanged analogs. This is attributed to the occurrence of different deactivation pathways in the exchanged analogs due to the presence of N-donor terminal or N/O-donor chelating aromatic ancillary ligands in the place of DMF terminal ligands in the pristine material. Overall, this work provides insights into the role of terminal and chelating ligands on the thermometric properties of mixed Eu–Tb MOFs and proposes a promising strategy to control and modulate their thermometric performances.

1. Introduction

Metal–organic frameworks (MOFs) have attracted a huge amount of attention because of their unique structures and topologies[1,2] and also due to their numerous applications, such as gas storage and separation,[2–4] magnetism,[5] chemical sensing,[6–10] drug delivery,[11] catalysis,[12,13] and more recently, luminescent thermometry.[14] Although a large variety of MOFs has been already reported, many efforts are currently devoted to the fine-tuning and control of their properties. To this end, post-synthetic modification (PSM), which involves the targeted alteration of the structure of a MOF after it has been synthesized, plays a key role in the development of functional materials exhibiting the desired properties.[15,16] Various types of modifications have been achieved including insertion/removal of guest molecules, changes of organic ligands, modifications of the metal ion coordination environment, or exchange of the metal ion(s) (transmetalation). Such modifications are preferable to proceed in a single-crystal-to-single-crystal (SCSC) fashion in order to obtain direct structural information about them through single-crystal X-ray crystallography.[17]

Temperature is a fundamental parameter that is necessary to accurately measure in various domains such as industrial manufacturing, monitoring processes, medicine, and safety.[14,18–20] Luminescence thermometry is currently appeared as a promising technique to obtain a precise measurement of temperature without any contact with the object. Lanthanide-based metal–organic frameworks (LnMOFs) are very promising candidates for use as luminescent thermometers due to their important advantages, including fast response, high accuracy, non-invasive nature, and high spatial resolution characteristics at the submicron scale where traditional methods are ineffective. Since 2012, when Cui et al.[21] published on the first ratiometric Eu–Tb MOF luminescent thermometers, many other Eu–Tb mixed compounds have been reported with various thermometric performances establishing luminescent MOFs as an important category of temperature sensing materials.[14,22–25]

Undoubtedly, the area of luminescent MOFs with application in temperature sensing dramatically evolves and one direction for its further progress is to take advantage of the PSM method to construct materials with finely tuned properties by varying the terminal or chelating ligands. In fact, different

A. Kourtellaris, A. J. Tasiopoulos
Department of Chemistry
University of Cyprus
Nicosia 1678, Cyprus
E-mail: atasio@ucy.ac.cy
W. Lafargue-Dit-Hauret, F. Massuyeau, C. Latouche, H. Serier-Brault
Nantes Université
CNRS
Institut des Matériaux de Nantes Jean Rouxel, IMN
Nantes F-44000, France
E-mail: camille.latouche@cnrs-imn.fr; helene.brault@cnrs-imn.fr
The ORCID identification number(s) for the author(s) of this article can be found under https://doi.org/10.1002/adom.202200484.

DOI: 10.1002/adom.202200484

studies, involving mainly mononuclear or dinuclear lanthanide complexes, highlighted the importance of the judicious choice of the ligand on the sensitivity of Ln^{3+}-based molecular thermometers.[26–28] In addition, some of these studies also evidenced the impact of the ligand on the shape of the calibration curve and relative thermal sensitivity curves.[26] To this end, it would be interesting to modify in a targeted way the coordination environment of the Ln^{3+} ion(s) of selected MOFs by exchanging their terminal ligands and investigate how selected structural alterations affect the thermometric performances of the exchanged MOF materials. However, this field is still in its infancy and many progresses are still necessary to reach maturity. The literature in this area, thus, includes only two studies involving a PSM that led to the turn-on of the photoluminescence and the temperature sensing capability of a non-luminescent pristine material[29] and the investigation of the thermometric performances of an Eu^{3+}-based MOF and its guest, as well as the guest and coordinated solvent molecule exchanged analogs.[30]

Herein, we discuss the thermometric properties of the rigid MOF $[Tb_{1.9}Eu_{0.1}(N\text{-}BDC)_3(DMF)_4]$ (**EuTb-NBDC**) (N-BDC = 2-amino-1,4-benzenedicarboxylate, DMF = *N*,*N*-dimethylformamide) which was found to exhibit a very good sensitivity for the medium temperatures (100 K < T < 293 K), with a maximum relative sensitivity (S_m) of 2.6% K^{-1} at 190 K being very competitive with the other mixed Eu–Tb MOFs operating in the same temperature range.[14] To investigate the role of peripheral ancillary ligands on the temperature sensing capability and finely tune the thermometry properties of this functional MOF, a series of SCSC exchanged analogs,[17] namely **EuTb-NBDC/Im** (Im = imidazole), **EuTb-NBDC/2mIm** (2mIm = 2-methyl-1H-imidazole), **EuTb-NBDC/mIma** (mIma = 5-methyl-1H-imidazole-4-carbaldehyde), and **EuTb-NBDC/m2hmp** (m2hmp = 3-methyl-2-(hydroxymethyl)pyridine) were synthesized by a controlled PSM process. The pristine **EuTb-NBDC** MOF and the exchanged derivatives exhibit analogous structures and coordination numbers of Ln^{3+} cations differing only in the type of the coordinated ancillary ligands. Interestingly, the investigation of the thermometry properties of the exchanged analogs revealed that they are sensitive at a lower temperature, with a thermal sensitivity around 2% K^{-1} at 140 K, that is, an offset of 50 K compared to the pristine MOF. Thus, the effect of controlled structural modifications on the thermometric properties of luminescent MOFs is investigated for the first time establishing the PSM method and single-crystal coordinating solvent exchange reactions as invaluable methods for the construction of a new generation of superior temperature sensors.

2. Structural and Chemical Characterization

The **EuTb-NBDC** MOF was prepared following a published procedure[31] with the difference that both $Eu(NO_3)_3 \cdot 5H_2O$ and $Tb(NO_3)_3 \cdot 5H_2O$ were used in the reaction mixture in a 5/95% molar ratio. It contains a $[Ln_2(NBDC)_3(DMF)_4]$ secondary building unit (SBU) with each Ln^{3+} ion connected to seven carboxylate O atoms of the $NBDC^{2-}$ ligands and two O atoms from terminal DMF molecules. This MOF platform was selected to investigate systematically the effect of the modification of the terminal/chelating ligands on its thermometry properties because: i) it is a luminescent MOF, ii) it exhibits a significant capability to exchange its terminally ligated DMF molecules with several organic molecules allowing the investigation of the thermometry properties of a variety of analogs involving a different degree of terminal ligands replacement, exchange of terminal by chelating ligands, as well as the exchange of terminal by chelating ligand accompanied by insertion of guest molecules,[17] and iii) the replacement of the terminal ligands is the main structural modification taking place upon the exchange reactions, whereas other important structural features (e.g., the coordination number of the metal ions, coordination geometry, and structural topology) remain essentially unaffected. In particular, the exchanged analogs **EuTb-NBDC/2mIm** (in which one terminal DMF molecule of the pristine material has been replaced by one terminal 2mIm ligand), **EuTb-NBDC/Im** (in which the two terminal DMF molecules have been replaced by two terminal Im ligands), **EuTb-NBDC/mIma** (in which the two terminal DMF molecules of the pristine material have been replaced by one chelating mIma ligand), and **EuTb-NBDC/m2hmp** (in which the two terminal DMF molecules of the pristine material have been replaced by one chelating m2hmp ligand and a 2-hmp (2-(hydroxymethyl)pyridine) ligand appears as guest molecule) were prepared from reactions of single-crystals of the pristine **EuTb-NBDC** with the corresponding organic molecules dissolved in $CHCl_3$ at 50 °C.[17] A representation of the exchange reactions and the secondary building units of the pristine and exchanged products is shown in **Figure 1**. These analogs contain terminal/chelating ligands exhibiting a variety of coordination modes and types of donor atoms (pristine **EuTb-NBDC**: two terminal ligands and 2 O donor atoms/Ln^{3+} ion; **EuTb-NBDC/2mIm**: two terminal ligands and 1 O/1 N donor atoms/Ln^{3+} ion; **EuTb-NBDC/Im**: two terminal ligands and 2 N donor atoms/Ln^{3+} ion, **EuTb-NBDC/mIma**, and **EuTb-NBDC/m2hmp**: one chelating ligand and 1 O/1 N donor atoms/Ln^{3+} ion) and could provide valuable insights for the role of the terminal/chelating ligands on the thermometry properties of Eu–Tb MOFs. The identity of the reported compounds was confirmed by the determination of the crystal structures of the pristine **EuTb-NBDC** and the exchanged **EuTb-NBDC/Im**, **EuTb-NBDC/2mIm**, **EuTb-NBDC/mIma**, and **EuTb-NBDC/m2hmp** MOFs (selected crystal data are reported in Table S1, Supporting Information), as well as by comparison of their experimental PXRD patterns with the simulated ones and also the experimental patterns of the corresponding Eu^{3+} compounds (Figures S1–S5, Supporting Information). Details about the synthesis and characterization (FTIR, TGA analyses) of the pristine **EuTb-NBDC** and the exchanged analogs are provided in Figures S6–S11, Supporting Information.

3. Photophysical Characterization

The photophysical properties of the pristine **EuTb-NBDC** and its exchanged analogs were studied in the solid-state (crystalline powders) by luminescence spectroscopy. Upon UV excitation at 395 nm, the room-temperature emission spectra of all samples display the main lines at 490 and 545 nm of Tb^{3+}, and

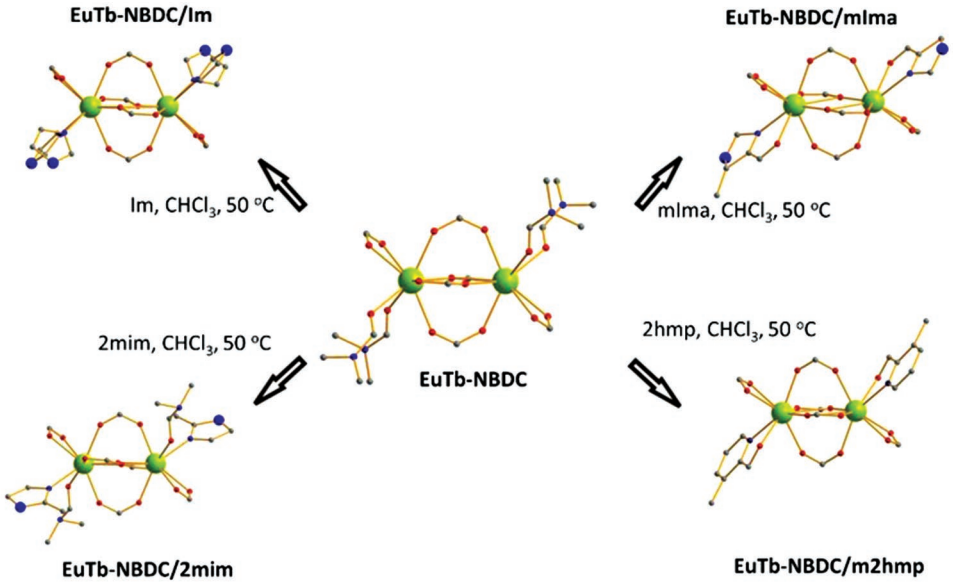

Figure 1. Single-crystal coordinating solvent exchange reactions of **EuTb-NBDC** that led to the formation of the exchanged derivatives **EuTb-NBDC/Im** (Im = imidazole), **EuTb-NBDC/2mIm** (2mIm = 2-methyl-1H-imidazole), **EuTb-NBDC/mIma** (mIma = 5-methyl-1H-imidazole-4-carbaldehyde), and **EuTb-NBDC/m2hmp** (m2hmp = 3-methyl-2-hydroxymethylpyridine) investigated in this study. Color code: green: mixed Eu/Tb site; red: O; blue: N; gray: C.

at 587, 611, and 695 nm for Eu^{3+}, attributed to the $^5D_4 \rightarrow {}^7F_{6\text{-}3}$ and the $^5D_0 \rightarrow {}^7F_{0\text{-}4}$ transitions of Tb^{3+} and Eu^{3+}, respectively (**Figure 2**).

Noticeably, the $^5D_4 \rightarrow {}^7F_5$ Tb^{3+} emission band (at 544 nm) is very weak for all compounds, which can be attributed to an efficient Tb^{3+}-to-Eu^{3+} energy transfer in the network and/or to a low energy difference between the triplet level of the ligand and the $^5D_4$ level of Tb^{3+} favoring the occurrence of a back transfer at room temperature. Excitation spectra monitored on the **EuTb-NBDC** compound evidence the presence of $^7F_6 \rightarrow {}^5D_4$ Tb^{3+} transition (at ≈490 nm) within the $^5D_0 \rightarrow {}^7F_2$ Eu^{3+} transition (Figure S12, Supporting Information), which confirms the occurrence of a Tb^{3+}-to-Eu^{3+} energy transfer in mixed Ln^{3+} compounds. Moreover, emission spectra contain also a broad emission band between 400 and 480 nm corresponding to the ligand emission, confirming the partial sensitization of both Tb^{3+} and Eu^{3+} ions by organic ligands. The insertion into the structure of the MOF of various organic aromatic ligands in the place of DMF molecules leads to small variations of this broad emission band, which corresponds actually to the resulting emission of both ligands (Figure S13, Supporting Information). Finally, under UV excitation at 395 nm, all samples exhibit red or orange emission color, as suggested by the CIE chromatic coordinates (*x*,*y*) (Table S2, Supporting Information).

Phosphorescence spectra of the Gd-NBDC and its exchanged analogs were also monitored at 77 K in order to estimate the energy of the triplet level (Figure S14, Supporting Information). Interestingly, two broad emission bands are observed on emission spectra at 77 K whereas a single band is present at 300 K (Figure S15, Supporting Information). To gain a deeper insight into the electronic transitions involved in these two bands, we conducted ab initio calculations on the NBDC and mIma molecules. For the NBDC system (Figure S16, Supporting Information), the $S_1 \rightarrow S_0$ fluorescence band is simulated with a maximum at ≈440 nm, while a broader $T_1 \rightarrow S_0$ phosphorescence band is found with a maximum at ≈550 nm. The obtained simulations reproduce well the experimental spectra and allow a possible explanation to be proposed for the difference between the emission spectra recorded at 77 and 300 K. In particular, the emission bands appearing in the photoluminescence spectrum recorded at 77 K are assigned to the $S_1 \rightarrow S_0$ fluorescence (maximum at ≈435 nm) and the $T_1 \rightarrow S_0$ phosphorescence (maximum at ≈535 nm). By increasing the temperature, the phosphorescence is quenched, resulting in the presence of a unique $S_1 \rightarrow S_0$ fluorescence band. This assumption was confirmed by the measurement at 300 K of the emission lifetime of Gd-NBDC, which leads to a decay time of 0.27 ns in good agreement with a fluorescence process (Figure S17, Supporting Information). The theoretical approach is in perfect agreement with the S_1 and T_1 values of 24 700 (405 nm) and 20 900 cm^{-1} (479 nm), respectively, reported in the literature for the NBDC ligand.[32] A similar situation was observed for the compound Gd-NBDC/mIma (Figure S18, Supporting Information). The slight bathochromic shift of the $T_1 \rightarrow S_0$ band and a relatively similar $S_1 \rightarrow S_0$ transition compared to the Gd-NBDC spectra suggested that the $NBDC^{2-}$ ligand plays a key role in the luminescence process, while the phosphorescence band results from the emission of both the $NBDC^{2-}$ and the mIma ligands. For the mIma molecule, the $T_1 \rightarrow S_0$ maximum was simulated at ≈530 nm, slightly lower than the experimental one that was shown at ≈545 nm. Finally, the T_1 levels of NBDC and mIma are very close, but considering the experimental data, the triplet level of the ancillary ligand is slightly lower.

Ancillary ligands have also an impact on the transition $^5D_0 \rightarrow {}^7F_2$ of Eu^{3+},[33,34] which is sensitive to the local symmetry of the Eu^{3+} ion. Since the parity-allowed magnetic dipole transition $^5D_0 \rightarrow {}^7F_1$ is independent of the ion surrounding, the integrated intensity ratio $I(^5D_0\text{-}\forall^7F_2)/I(^5D_0\text{-}^7F_1)$ can be considered as an indicator of the local environment of Eu^{3+}. Consequently,

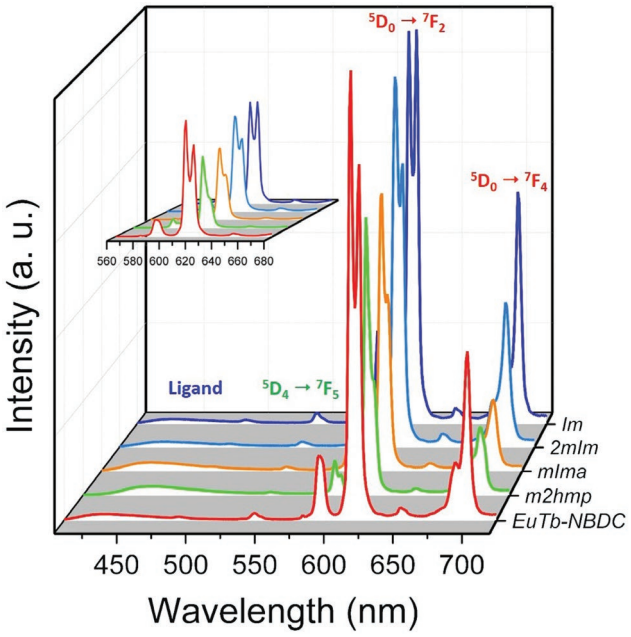

Figure 2. Room-temperature emission spectra of compounds **EuTb-NBDC, EuTb-NBDC/m2hmp**, **EuTb-NBDC/mIma**, **EuTb-NBDC/2mIm,** and **EuTb-NBDC/Im** monitored at 395 nm. A zoom of the $^5D_0 \forall {}^7F_2$ Eu^{3+} transition is depicted in the inset (Eu^{3+} and Tb^{3+} transitions are indicated using red and green color fonts, respectively).

the calculated intensity ratio varies from 5.15 to 7.22 for the pristine **EuTb-NBDC** and the exchanged analogs (Figure S19, Supporting Information), as expected on the basis of the structural variations in this family of analogous MOFs due to the presence of different terminal/chelating ligands in each compound.[17] Furthermore, the exchange of the terminal ligands also imposes changes in the $^5D_0$ decay time, monitored at 614 nm, whereas the $^5D_4$ decay time (at 545 nm) could not be measured due to a very low value (Table S2, Supporting Information). The quantum yields of the pristine **EuTb-NBDC** MOF and the exchanged derivatives were also found to be affected by terminal ligands exchange with a variation of ϕ from 17.8% in **EuTb-NBDC** to 25.4%, 11.8%, 3.6%, and 2.4% in **EuTb-NBDC/Im**, **EuTb-NBDC/2mIm**, **EuTb-NBDC/mIma**, and **EuTb-NBDC/m2hmp**, respectively (Table S2, Supporting Information).

4. Luminescence Thermometry

The application of **EuTb-NBDC** and its exchanged derivatives as ratiometric luminescent thermometers was investigated using the emission spectra in the 80–300 K range. The integrated areas of the $^5D_4 \rightarrow {}^7F_5$ (I_{Tb}) and $^5D_0 \rightarrow {}^7F_2$ (I_{Eu}) emissions were used to define the thermometric parameter as $\Delta = I_{Tb}/I_{Eu}$. The I_{Tb} and I_{Eu} areas were integrated using the emission spectra in the 530–560 nm and 602–633 nm intervals, respectively. Five consecutive emission spectra were recorded for each temperature, and the mean values of the areas ± standard deviation (SD) were reported.

The temperature dependence of **EuTb-NBDC** emission spectra is presented in Figure S20, Supporting Information, and the thermal dependence of integrated intensities in **Figure 3**a,

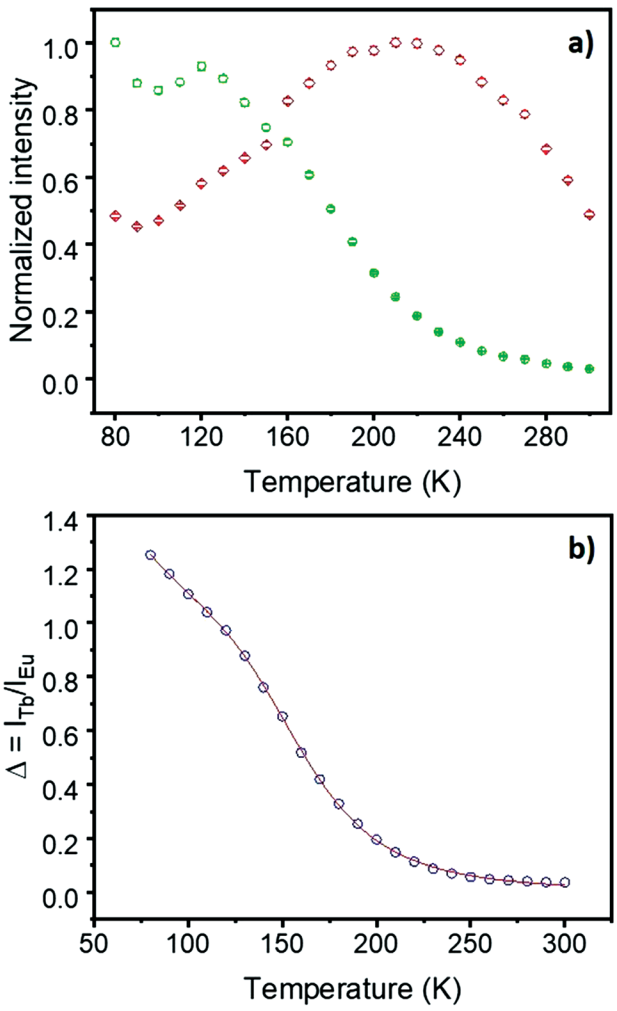

Figure 3. a) Temperature dependence of I_{Tb} (green) and I_{Eu} (red) in **EuTb-NBDC**. b) Temperature dependence of Δ in **EuTb-NBDC** in the 80–300 K range. The red line represents the calibration curve obtained by the best fit of the experimental points to Equation (1) ($r^2 > 0.999$).

which clearly demonstrates the distinct temperature dependence of the Tb^{3+} $^5D_4 \rightarrow {}^7F_5$ and Eu^{3+} $^5D_0 \rightarrow {}^7F_2$ integrated emissions. Thus, the Tb^{3+} emission decreases in the whole temperature range and at 300 K reaches 3% of its 80 K intensity, whereas the Eu^{3+} emission increases 222% from 80 to 210 K where it reaches the maximum, and then decreases 204% up to 300 K. The thermometric parameter Δ (Figure 3b) is depicted according to the temperature in the 80–300 K range and may be described by the phenomenological Mott–Seitz expression involving two non-radiative recombination channels in competition (assuming a temperature dependence of the Eu^{3+} emission smaller than that of the Tb^{3+} emission), Figure 3a).

$$\Delta(T) = \frac{\Delta_0}{1 + \alpha_1 \exp\left(-\frac{\Delta E_1}{k_B T}\right) + \alpha_2 \exp\left(-\frac{\Delta E_2}{k_B T}\right)} \quad (1)$$

where Δ_0 is the Δ parameter at T → 0 K, $\alpha = W_0/W_R$ is the ratio between the non-radiative and radiative decay rates in the

limit of T → 0 K, and ΔE_1 and ΔE_2 are the activation energies for the two non-radiative channels. Fitting the experimental Δ values to Equation (1) yields $\Delta_0 = 1.6 \pm 0.2$, $\alpha_1 = 4660 \pm 512$, $\Delta E_1 = 918 \pm 22$ cm^{-1}, $\alpha_2 = 2.5 \pm 0.4$, and $\Delta E_2 = 121 \pm 36$ cm^{-1}, pointing out that the temperature dependence of the ratiometric parameter Δ is strongly dominated by the temperature dependence of the first deactivation channel. The first non-radiative recombination channels (ΔE_1 = 918 cm^{-1}) can be tentatively ascribed to the back-energy transfer from the $^5D_4$ level of Tb^{3+} ion (20 500 cm^{-1})[14] to the triplet level of the $NBDC^{2-}$ ligand (T_1 = 20 900 cm^{-1}),[32] while the second deactivation pathway (ΔE_2 = 121 cm^{-1}) can be assigned to the ligand-mediated Tb^{3+}-to-Eu^{3+} energy transfer.[35] The latter pathway can explain the opposite variation of I_{Tb} and I_{Eu} in the 80–210 K range where I_{Tb} decreases and I_{Eu} increases, confirming the occurrence of a Tb^{3+}-to-Eu^{3+} energy transfer. The corresponding relative thermal sensitivity is defined as $S_r = |\partial\Delta/\partial T|/\Delta$ and used as a figure of merit to compare the performance of distinct systems,[14,18,22] is plotted in **Figure 4**. Thus, as a luminescent ratiometric thermometer, the pristine **EuTb-NBDC** material exhibits a very good sensitivity for the medium temperatures (100 K < T < 293 K), with a maximum relative sensitivity (S_m) of 2.6% K^{-1} at 190 K. The pristine material is very competitive with the other mixed EuTb MOFs operating in the same temperature range such as $Tb_{0.9931}Eu_{0.0069}$(dmbdc) (S_m = 1.15% K^{-1} at 200K),[21] $[Tb_{0.99}Eu_{0.01}(hfa)_3(dpbp)]_n$ (S_m = 0.52% K^{-1} at 200K),[36] or $Tb_{0.98}Eu_{0.02}$(BDC)(DSTP) (S_m = 3.9% K^{-1} at 200K).[37]

For this reason, four exchanged analogs differing from the pristine MOF mainly in their peripheral ligation were isolated aiming to fine tune the thermometry properties of the pristine MOF through controlled structural modifications and investigate the role of the terminal/chelating ligands on the thermometric properties, that is, temperature sensing range and relative thermal sensitivity. The thermometric properties of the four exchanged analogs of **EuTb-NBDC**, were also thoroughly studied. Their Tb^{3+} emission decreases in the whole temperature range to be almost totally quenched at 300 K. For

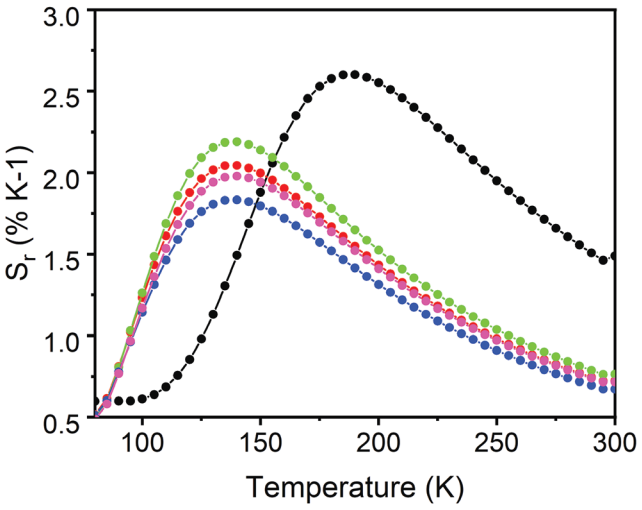

Figure 4. Relative thermal sensitivity of **EuTb-NBDC** (black line), **EuTb-NBDC/m2hmp** (red line), **EuTb-NBDC/mIma** (pink line), **EuTb-NBDC/2mIm** (green line), and **EuTb-NBDC/Im** (blue line).

Table 1. Fitting parameters of Equation (1) to the experimental Δ(T) for **EuTb-NBDC/Im**, **EuTb-NBDC/2mIm**, **EuTb-NBDC/mIma**, and **EuTb-NBDC/m2hmp**. Only a single non-radiative recombination channel was considered.

	Im	2mIm	mIma	m2hmp
Δ_0	0.698 ± 0.009	0.463 ± 0.004	0.194 ± 0.002	0.70 ± 0.01
α	118 ± 10	229 ± 15	149 ± 9	174 ± 34
ΔE_1	435 ± 10	481 ± 8	451 ± 7	456 ± 22
r^2	0.998	0.999	0.999	0.995

EuTb-NBDC/Im and **EuTb-NBDC/2mIm**, the Eu^{3+} emission displays similar behavior to the one shown for the pristine **EuTb-NBDC**, with an increase of the intensity up to 190 K, and a decrease for T > 190 K (Figures S21 and S22, Supporting Information). On the other hand, the Eu^{3+} emission of **EuTb-NBDC/mIma** and **EuTb-NBDC/m2hmp** continually decreases in the whole temperature range (Figures S23 and S24, Supporting Information). For all samples, the thermometric parameter Δ (Figure S25, Supporting Information) may be also described by the phenomenological Mott–Seitz expression, but with unique non-radiative recombination channels; the fitting parameters are reported in **Table 1**. For compound **EuTb-NBDC/mIma**, the hypothesis to neglect the thermal quenching of I_{Eu} and to consequently apply the Mott–Seitz in Equation (1) appears questionable since the thermal quenching of I_{Eu} reaches 80% in the investigated temperature range. For this reason, attempts to simulate the calibration curve, $\Delta = f(T)$, by considering one deactivation pathway on each Ln^{3+} emitter, were performed using the non-simplified Mott–Seitz equation.[14] However, these attempts led to low-quality fits with inaccurate fitting parameters (the standard deviations were higher than the obtained values). Consequently, the fitting parameters obtained for the compound **EuTb-NBDC/mIma** are also reported in Table 1 but it is indicated to be considered with caution.

For all exchanged analogs, the activation energy for the non-radiative channel exhibit similar values, ranging from 430 to 480 cm^{-1}, which is almost half the value obtained for the pristine **EuTb-NBDC**. The role of the terminal/chelating ligands on thermometric properties has never been investigated so far. Although there are reports involving the investigation of the thermometric properties on mixed-ligand MOFs, these did not allow the investigation of the effect of the terminal/chelating or bridging ligands on the thermometric properties either because the structures of the investigated analogs exhibited major differences (i.e., in topology, dimensionality)[37] or due to the existence of several structural differentiations in the investigated materials.[30] In coordination complexes containing two different ligands,[36–38] it has been proposed that the deactivation pathways occur through a ligand-to-ligand charge-transfer excited state, especially when one ligand displays a longer π-conjugation, which stabilizes the excited states of both ligands, allowing the formation of a ligand-to-ligand charge transfer (LLCT) band.[38,39] However, for the **EuTb-NBDC** exchanged analogs, both ligands, namely the $NBDC^{2-}$ and the N-donor terminal or N/O-donor chelating ligands, exhibit the same π–system, which indicates that no LLCT occurs. In fact, the absence of the LLCT band for the exchanged analogs was

confirmed by diffuse reflectance measurements (Figure S26, Supporting Information).

A series of mixed Eu–Tb complexes with various ligands, exhibiting different triplet levels were reported by Carlos and co-workers.[27] It was proposed that the positioning of the triplet level at high energy prevents the $^5D_4$-to-ligand energy back transfer while ligands with triplet level at lower energy favor this energy back transfer. By considering our theoretical calculations on the **mIma** ligand, and the phosphorescence spectra of Gd^{3+} counterparts, the triplet level of our exchanged terminal ligands tends to be placed at lower energy than the T_1 level of the $NBDC^{2-}$ ligand. Thus, in exchanged compounds, the thermometric properties might be dictated by the $^5D_4$-to-exchanged ligand energy back transfer while in the pristine material they are governed by the $^5D_4$-to-$NBDC^{2-}$ energy back transfer. It thus becomes clear that the insertion of an ancillary aromatic ligand in the exchanged analogs induces competition between the different ligands surrounding the Ln^{3+} emitters, implying a modulation of non-radiative pathways, and consequently a variation of thermometric properties.

The plot of the corresponding thermal sensitivity S_r for all exchanged analogs (Figure 4) reveals that S_m slightly decreased to ≈1.8% K^{-1} – 2.2% K^{-1} and the T_m is shifted to around 140 K. These sensitivity values are very competitive with those known from the literature examples of luminescent ratiometric MOF-based thermometers operating in the medium range (**Table 2**). By considering that a luminescent thermometer is useable in practice when the S_r value is superior to 1% K^{-1},[40] the compound **EuTb-NBDC** can be easily used in the 125–300 K range, while the exchanged analogs are sensitive in the 95–245 K. Thus, the operating temperature range is modified upon exchange of ancillary ligands of **EuTb-NBDC** MOF. The structural analogies of the inserted ligands (imidazole and its derivatives **2mIm** and **mIma** and the pyridine derivative **m2hmp**) in the exchanged analogs can explain the close ΔE values from the Mott–Seitz fits and the similarity of their thermometric performances.

Table 2. Overview of the maximum relative sensitivity S_m for mixed Eu–Tb MOFs displaying a thermal sensitivity around 200 K.

Materials	S_m [% K^{-1}]	T_m [K]
EuTb-dmbdc[21]	1.15	200
EuTb@UiO-67-bpydc[54]	3.01	180
$[TbEu(hfa)_3(dpbd)]_n$[36]	0.52	200
EuTb-BDC-DSTP[37]	3.9	200
$[EuTb(L)_2(NO_3)_2]$ Cl $2H_2O$[55]	0.34	200
EuTb-cpna[56]	2.55	131
EuTb-bpydc[56]	2.59	179
EuTb-NBDC	2.6	190
EuTb-NBDC/mIma	1.98	140
EuTb-NBDC/m2hmp	2.04	140
EuTb-NBDC/2mIm	2.19	140
EuTb-NBDC/Im	1.83	140

dmbdc, 2,5-dimethoxy-1,4-benzendicarboxylic acid; bpydc, 2,2′-bipyridyl dicarboxylic acid; hfa, hexafluoro acetylacetonato; dpbd, 4,4′-bis(diphenylphosphoryl)biphenyl; BDC, 1,4-benzenedicarboxylic acid; DSTP, (2,2′:6′,2″-terpyridin-4′-yl)-benzenedisulfonic acid; L, 1,4-bis(pyridinil-4-carboxylato)-1,4-dimethylbenzene; cpna, (4-carboxyphenyl) nicotinic acid).

The temperature uncertainty of the thermometers is calculated using the following expression[41]

$$\delta T = \frac{1}{S_r}\frac{\delta\Delta}{\Delta} \quad (2)$$

where $\delta\Delta/\Delta$ is the relative uncertainty on the thermometric parameter, which depends on the acquisition setup and in this study was assumed to be 0.2% and δT defines the minimum temperature change that may be ascertained in a specific measurement. For **EuTb-NBDC**, a minimum temperature uncertainty of 0.08 K was obtained at 190 K and a maximum of 0.33 K in the cryogenic range ($T < 100$ K). For exchanged analogs, an average minimum uncertainty of 0.1 K was obtained at 140 K and a maximum around 0.4 K in the cryogenic range ($T < 100$ K) (Figure S27, Supporting Information).

Finally, to evaluate whether the material could be used as a reliable thermometer, cycle tests were performed on **EuTb-NBDC**, which is the more sensitive thermometer of the series, and the repeatability was calculated according to Equation (3).[14]

$$R = 1 - \frac{\max|\Delta_c - \Delta_i|}{\Delta_c} \quad (3)$$

where Δ_C is the mean thermometric parameter, and Δ_i is the value of each measurement of the thermometric parameter. Then, four cycles between 140 and 240 K were carried out (Figure S28, Supporting Information) to obtain a repeatability $R > 95\%$, which confirms the robustness of the materials for an application as luminescent thermometer.

5. Conclusions

The effect of the presence of various terminal or chelating ligands in the structure of **EuTb-NBDC** MOF and its exchanged analogs on their thermometry properties has been investigated in detail. Among all parameters that can affect the thermometric performances of a mixed Eu–Tb MOF, the role of the terminal ligands has not been investigated previously mainly because it is not straightforward to exchange the terminal or chelating ligands of MOFs without performing additional structural alterations. Herein, by using a post-synthesis modification method, we succeeded in exchanging the terminal DMF molecules of **EuTb-NBDC** MOF with other terminal or chelating organic aromatic ligands exhibiting various types of donor atoms in a controlled manner that avoided undesirable structural alterations, especially regarding the Ln^{3+} coordination polyhedra. The insertion of these ligands in the structure of **EuTb-NBDC** MOF led to the modification of the deactivation channels since they display a lower T_1 excited state than that of $NBDC^{2-}$, as proved by theoretical calculations. In addition, the pristine material, **EuTb-NBDC**, exhibited a high thermal sensitivity of 2.6% K^{-1} at 190 K while its exchanged analogs were shown to be sensitive at a lower temperature, with thermal sensitivity of around 2% K^{-1} at 140 K, that is, an offset of 50 K. Overall, this investigation highlights the role of PSM method

for the modulation of the thermometry properties of well-performing materials and the design of new performant LnMOF luminescent thermometers.

6. Experimental Section

Materials Synthesis: Reagent-grade chemicals were obtained from Aldrich and used without further purification. **Eu-NBDC** (NBDC = 2-amino-1,4-benzenedicarboxylate) compound and its Gd^{3+} analog were prepared as described elsewhere.[17]

$[Tb_{1.9}Eu_{0.1}(N\text{-}BDC)_3(DMF)_4]$ (**EuTb-NBDC**): Compound **EuTb-NBDC** was prepared by following the same procedure as that of **Eu-NBDC**[31] except that in the place of $Eu(NO_3)_3{\cdot}5H_2O$, mixed lanthanide salts of $Eu(NO_3)_3{\cdot}5H_2O$ and $Tb(NO_3)_3{\cdot}5H_2O$ in a 5/95% molar ratio was used. Elemental analysis calculated for **$Tb_{1.9}Eu_{0.1}$-NBDC**·2DMF·$2H_2O$ ($C_{42}H_{61}Eu_{0.1}Tb_{1.9}N_9O_{20}$): C 37.95; H 4.63; N 9.48; found: C 37.73; H 4.49; N 9.66. The metal ion content was determined by inductively coupled plasma atomic emission spectrometry (ICP-AES) and provided a Tb^{3+}/Eu^{3+} ratio of 0.951/0.049.

$Tb_{1.9}Eu_{0.1}$-NBDC/X (X = Imidazole (Im), 2-Methyl-1H-imidazole (2mim), 5-Methyl-1H-imidazole-4-carbaldehyde (mIma)): Single crystals of **$Tb_{1.9}Eu_{0.1}$-NBDC** (0.03–0.04 mmol) and a solution of X (0.32–0.59 mmol) in $CHCl_3$ (5 mL) were mixed in a 23 mL Teflon-lined stainless-steel autoclave. The autoclave was sealed and placed in an oven operated at 50 °C, remained undisturbed at this temperature for 2 days, and then was allowed to cool at room temperature. The crystals of **$Tb_{1.9}Eu_{0.1}$-NBDC/X** were isolated by filtration and dried in the air. ICP-AES studies provided a Tb^{3+}/Eu^{3+} ratio within the range of 0.962/0.038–0.938/0.062 for the exchanged analogs.

Elemental analysis calculated for **$Tb_{1.9}Eu_{0.1}$-NBDC/Im**·0.1DMF·$3.5H_2O$ ($C_{36.3}H_{38.7}Eu_{0.1}Tb_{1.9}N_{11.1}O_{15.6}$): C 36.42; H 3.26; N 12.99; found: C 36.70; H 2.99; N 13.22.

Elemental analysis calculated for **$Tb_{1.9}Eu_{0.1}$-NBDC/2mIm**·0.2DMF·$5.5H_2O$ ($C_{38.6}H_{53.4}Eu_{0.1}Tb_{1.9}N_{9.2}O_{19.7}$): C 36.26; H 4.21; N 10.08; found: C 36.42; H 4.40; N 10.28.

Elemental analysis calculated for **$Tb_{1.9}Eu_{0.1}$-NBDC/mIma**·0.1DMF·$8H_2O$ ($C_{34.3}H_{43.7}Eu_{0.1}Tb_{1.9}N_{7.1}O_{22.1}$): C 33.60; H 3.59; N 8.11; found: C 33.79; H 3.41; N 8.28.

$Tb_{1.9}Eu_{0.1}$-NBDC/m2hmp (m2hmp = 3-Methyl-2-(hydroxymethyl) pyridine): Single crystals of **$Tb_{1.9}Eu_{0.1}$-NBDC** (0.04 mmol) and a solution of **2hmp** (5.18 mmol) in $CHCl_3$ (5 mL) were mixed in a 23 mL Teflon-lined stainless steel autoclave. The autoclave was sealed and placed in an oven operated at 50 °C, remained undisturbed at this temperature for 2 days, and then was allowed to cool at room temperature. The crystals of **$Tb_{1.9}Eu_{0.1}$-NBDC/m2hmp** were isolated by filtration and dried in the air. ICP-AES studies provided a Tb^{3+}/Eu^{3+} ratio of 0.962/0.038.

Elemental analysis calculated for **$Tb_{1.9}Eu_{0.1}$-NBDC/m2hmp**·0.05DMF·$5H_2O$·2hmp ($C_{44.15}H_{50.35}Eu_{0.1}Tb_{1.9}N_{6.05}O_{20.05}$): C 40.68; H 3.89; N 6.50; found: C 41.05; H 3.68; N 6.67.

Single-Crystal X-ray Crystallography: Single-crystal X-ray diffraction data for the pristine **EuTb-NBDC** and the exchanged analogs **EuTb-NBDC/Im**, **EuTb-NBDC/2mIm**, **EuTb-NBDC/mIma**, and **EuTb-NBDC/m2hmp** were collected on a Rigaku Oxford Diffraction Supernova diffractometer, equipped with a CCD area detector utilizing Mo Kα (λ = 0.71073 Å) or Cu Kα (λ = 1.5418 Å) radiation. Suitable crystals were attached to glass fibers using paratone-N oil and transferred to a goniostat where they were cooled for data collection. Empirical absorption corrections (multiscan based on symmetry-related measurements) were applied using CrysAlis RED software.[42] The same software package was used for data collection, cell refinement, and data reduction. The structures were solved by direct methods using either SHELXT or SHELXS,[43,44] via the WinGX interface. They were refined on F^2 using full-matrix least-squares with SHELXL-14.1. The non-H atoms were treated anisotropically, whereas the aromatic H atoms were placed in calculated, ideal positions and refined as riding on their respective carbon atoms. Electron density contributions from disordered guest molecules were handled using the SQUEEZE procedure from the PLATON software suite.[45] PLATON and DIAMOND[46] were used for geometric calculations. Selected crystal data for the reported structures are summarized in Table S1, Supporting Information. CCDC 2167474 (**EuTb-NBDC**), 2167475 (**EuTb-NBDC/Im**), 2167476 (**EuTb-NBDC/2mIm**), 2167477 (**EuTb-NBDC/mIma**), and 2167473 (**EuTb-NBDC/m2hmp**) contain the supplementary crystallographic data for this paper. These data can be obtained free of charge from The Cambridge Crystallographic Data Center via www.ccdc.cam.ac.uk/data-request/cif

Physical Measurements: Elemental analysis (C, H, and N) was performed by the in-house facilities of the University of Cyprus, Chemistry Department. IR spectra were recorded on ATR in the 4000–700 cm^{-1} range using a Shimadzu Prestige – 21 spectrometer. Powder X-ray diffraction patterns were recorded on a Rigaku Miniflex 6G X-ray diffractometer (Cu Kα radiation, λ = 1.5418 Å). Thermal stability studies were performed with a Shimadzu TGA 50 thermogravimetric analyzer. Room-temperature UV–vis diffuse reflectance spectra were recorded on a Perkin Elmer Lambda 1050 for each finely ground sample. For room-temperature spectra, the spectrophotometer was equipped with an integrating sphere coated with Spectralon, a highly reflecting fluoropolymer. The absorption (α/S) values were calculated from the reflectance using the Kubelka–Munk transformation: $\alpha/S = (1 - R)^2/2R$, where R is the reflectance at the given wavelength, α is the absorption coefficient, and S is the scattering coefficient. The S value was supposed to be particle size independent since the grains size was larger than a few micrometers. Photoluminescence spectra were recorded on a Jobin–Yvon Fluorolog 3 fluorometer equipped with a photomultiplier (excitation source: 450 W Xe arc lamp) using the front face acquisition mode. The emission spectra were corrected for detection and optical spectral response of the spectrofluorimeter and the excitation spectra were weighed for the spectral distribution of the lamp intensity using a photodiode reference detector. The temperature-dependent photoluminescence measurements were recorded on the same spectrometer controlling the temperature by a cryostat coupled with the Fluorolog cooled by liquid nitrogen. Lifetimes measurements were measured with the same equipment but the excitation was performed by a UV Xenon flash tube while the time-dependence of the emission was recorded with the photomultiplier.

Time-resolved photoluminescence (TRPL) experiments were carried out with a regenerative amplified femtosecond Ti:sapphire laser system (Spectra Physics Hurricane X) frequency doubled to obtain an excitation line λ_{exc} = 400 nm. The transient signals were spectrally dispersed into a Princeton Instruments SP2300 imaging Acton spectrograph and temporally resolved with a high dynamic range Hamamatsu C7700 streak camera.

Computational Details: First-principles calculations based on density functional theory (DFT) were performed using the Gaussian16 package.[47] The B3LYP functional[48–50] and 6-31++G(d,p) basis set were employed during the simulations in conjunction with the polarizable continuum model (PCM)[51,52] to take into account solvent effects (THF). Geometry relaxations were carried out on the singlet S_0 and T_1 triplet states of NBDC and mIma systems. The S_1 state of each compound was investigated from the singlet S_0 state by the use of the TD-DFT[53] approach. Photoluminescence spectra were simulated by taking into account the vibrational contributions to the electronic transitions.

Supporting Information

Supporting Information is available from the Wiley Online Library or from the author.

Acknowledgements

W.L.-D.-H. and C.L. thank the CCIPL (Centre de Calculs Intensifs des Pays de la Loire) for the computational facilities. A.J.T. and A.K. thank

the Cyprus Research and Innovation Foundation Research Grant "EXCELLENCE/1216/0076," which is co-funded by the Republic of Cyprus and the European Regional Development Fund.

Conflict of Interest

The authors declare no conflict of interest.

Data Availability Statement

The data that support the findings of this study are available on request from the corresponding author. The data are not publicly available due to privacy or ethical restrictions.

Keywords

lanthanide ions, luminescence thermometry, metal–organic frameworks, post-synthetic modification, temperature sensing

Received: March 1, 2022
Revised: June 7, 2022
Published online: July 25, 2022

[1] M. Eddaoudi, D. B. Moler, H. Li, B. Chen, T. M. Reineke, M. O'Keeffe, O. M. Yaghi, *Acc. Chem. Res.* **2001**, *34*, 319.
[2] M. Eddaoudi, J. Kim, N. Rosi, D. Vodak, J. Wachter, M. O'Keeffe, O. M. Yaghi, *Science* **2002**, *295*, 469.
[3] X. Zhang, Z. Chen, X. Liu, S. L. Hanna, X. Wang, R. Taheri-Ledari, A. Maleki, P. Li, O. K. Farha, *Chem. Soc. Rev.* **2020**, *49*, 7406.
[4] N. S. Bobbitt, M. L. Mendonca, A. J. Howarth, T. Islamoglu, J. T. Hupp, O. K. Farha, R. Q. Snurr, *Chem. Soc. Rev.* **2017**, *46*, 3357.
[5] P. Dechambenoit, J. R. Long, *Chem. Soc. Rev.* **2011**, *40*, 3249.
[6] E. A. Dolgopolova, A. M. Rice, C. R. Martin, N. B. Shustova, *Chem. Soc. Rev.* **2018**, *47*, 4710.
[7] H. Wang, W. P. Lustig, J. Li, *Chem. Soc. Rev.* **2018**, *47*, 4729.
[8] X.-Y. Xu, B. Yan, *ACS Appl. Mater. Interfaces* **2015**, *7*, 45.
[9] J. Min, X.-L. Qu, B. Yan, *Sens. Actuators B Chem.* **2019**, *300*, 126985.
[10] A. Douvali, A. C. Tsipis, S. V. Eliseeva, S. Petoud, G. S. Papaefstathiou, C. D. Malliakas, I. Papadas, G. S. Armatas, I. Margiolaki, M. G. Kanatzidis, T. Lazarides, M. J. Manos, *Angew. Chem., Int. Ed.* **2015**, *127*, 1671.
[11] P. Horcajada, R. Gref, T. Baati, P. K. Allan, G. Maurin, P. Couvreur, G. Férey, R. E. Morris, C. Serre, *Chem. Rev.* **2012**, *112*, 1232.
[12] S. L. Anderson, P. G. Boyd, A. Gładysiak, T. N. Nguyen, R. G. Palgrave, D. Kubicki, L. Emsley, D. Bradshaw, M. J. Rosseinsky, B. Smit, K. C. Stylianou, *Nat. Commun.* **2019**, *10*, 1612.
[13] R. J. Drout, L. Robison, O. K. Farha, *Coord. Chem. Rev.* **2019**, *381*, 151.
[14] J. Rocha, C. D. S. Brites, L. D. Carlos, *Chem. Eur. J.* **2016**, *22*, 14782.
[15] K. K. Tanabe, S. M. Cohen, *Chem. Soc. Rev.* **2011**, *40*, 498.
[16] S. K. Ghosh, J.-P. Zhang, S. Kitagawa, *Angew. Chem., Int. Ed.* **2007**, *46*, 7965.
[17] E. J. Kyprianidou, T. Lazarides, S. Kaziannis, C. Kosmidis, G. Itskos, M. J. Manos, A. J. Tasiopoulos, *J. Mater. Chem. A* **2014**, *2*, 5258.
[18] M. D. Dramicanin, *J. Appl. Phys.* **2020**, *128*, 040902.
[19] R. Piñol, J. Zeler, C. D. S. Brites, Y. Gu, P. Téllez, A. N. Carneiro Neto, T. E. Da Silva, R. Moreno-Loshuertos, P. Fernandez-Silva, A. I. Gallego, L. Martinez-Lostao, A. Martínez, L. D. Carlos, A. Millán, *Nano Lett.* **2020**, *20*, 6466.
[20] M. Quintanilla, L. M. Liz-Marzán, *Nano Today* **2018**, *19*, 126.
[21] Y. Cui, H. Xu, Y. Yue, Z. Guo, J. Yu, Z. Chen, J. Gao, Y. Yang, G. Qian, B. Chen, *J. Am. Chem. Soc.* **2012**, *134*, 3979.
[22] C. D. S. Brites, P. P. Lima, N. J. O. Silva, A. Millán, V. S. Amaral, F. Palacio, L. D. Carlos, *New J. Chem.* **2011**, *35*, 1177.
[23] V. Trannoy, A. N. Carneiro Neto, C. D. S. Brites, L. D. Carlos, H. Serier-Brault, *Adv. Opt. Mater.* **2021**, *9*, 2001938.
[24] D. Zhao, X. Rao, J. Yu, Y. Cui, Y. Yang, G. Qian, *Inorg. Chem.* **2015**, *54*, 11193.
[25] Y. Yang, Y. Wang, Y. Feng, X. Song, C. Cao, G. Zhang, W. Liu, *Talanta* **2020**, *208*, 3.
[26] L. Bellucci, G. Bottaro, L. Labella, V. Causin, F. Marchetti, S. Samaritani, D. B. Dell'Amico, L. Armelao, *Inorg. Chem.* **2020**, *59*, 18156.
[27] C. D. S. Brites, P. P. Lima, L. D. Carlos, *J. Lumin.* **2016**, *169*, 497.
[28] T. Y. Popelensky, V. V. Utochnikova, *Dalton Trans.* **2020**, *49*, 12156.
[29] R. M. Abdelhameed, D. Ananias, A. M. S. Silva, J. Rocha, *Eur. J. Inorg. Chem.* **2019**, *2019*, 1354.
[30] J. De Bellis, L. Bellucci, G. Bottaro, L. Labella, F. Marchetti, S. Samaritani, D. Belli Dell'Amico, L. Armelao, *Dalton Trans.* **2020**, *49*, 6030.
[31] C. A. Black, J. S. Costa, W. T. Fu, C. Massera, O. Roubeau, S. J. Teat, G. Aromí, P. Gamez, J. Reedijk, *Inorg. Chem.* **2009**, *48*, 1062.
[32] A. Gamonal, C. Sun, A. L. Mariano, E. Fernandez-Bartolome, E. Guerrero-Sanvicente, B. Vlaisavljevich, J. Castells-Gil, C. Marti-Gastaldo, R. Poloni, R. Wannemacher, J. Cabanillas-Gonzalez, J. S. Costa, *J. Phys. Chem. Lett.* **2020**, *11*, 3362.
[33] K. Binnemans, *Coord. Chem. Rev.* **2015**, *295*, 1.
[34] X. Y. Xu, B. Yan, *ACS Appl. Mater. Interfaces* **2015**, *7*, 721.
[35] I. N'Dala-Louika, D. Ananias, C. Latouche, R. Dessapt, L. D. Carlos, H. Serier-Brault, *J. Mater. Chem. C* **2017**, *5*, 10933.
[36] K. Miyata, Y. Konno, T. Nakanishi, A. Kobayashi, M. Kato, K. Fushimi, Y. Hasegawa, *Angew. Chem., Int. Ed.* **2013**, *52*, 6413.
[37] Y. Wei, R. Sa, Q. Li, K. Wu, *Dalton Trans.* **2015**, *44*, 3067.
[38] Y. Hasegawa, Y. Kitagawa, *J. Mater. Chem. C* **2019**, *7*, 7494.
[39] P. P. Ferreira da Rosa, T. Nakanishi, Y. Kitagawa, T. Seki, H. Ito, K. Fushimi, Y. Hasegawa, *Eur. J. Inorg. Chem.* **2018**, *2018*, 2031.
[40] A. Bednarkiewicz, L. Marciniak, L. D. Carlos, D. Jaque, *Nanoscale* **2020**, *12*, 14405.
[41] C. D. S. Brites, A. Millán, L. D. Carlos, in *Handbook on the Physics and Chemistry of Rare Earths*, Vol. *49* (Eds: J.-C. Bünzli, V. K. Pecharsky), Elsevier, **2016**, Ch. 281.
[42] *CrysAlisPro*, Oxford Diffraction/Agilent Technologies UK Ltd, Yarnton, UK.
[43] G. M. Sheldrick, *SHELXL-2014/7, Program for Refinement of Crystal Structures*, University of Göttingen, Göttingen, Germany **2014**.
[44] G. M. Sheldrick, *Acta Crystallogr. A* **2008**, *64*, 112.
[45] A. L. Spek, *J. Appl. Crystallogr.* **2003**, *36*, 7.
[46] K. Brandenburg, *DIAMOND, Version 2003,2001d*, Crystal Impact GbR, Bonn, Germany **2006**.
[47] M. J. Frisch, G. W. Trucks, H. B. Schlegel, G. E. Scuseria, M. A. Robb, J. R. Cheeseman, G. Scalmani, V. Barone, G. a. Petersson, H. Nakatsuji, X. Li, M. Caricato, a. V. Marenich, J. Bloino, B. G. Janesko, R. Gomperts, B. Mennucci, H. P. Hratchian, J. V. Ortiz, a. F. Izmaylov, J. L. Sonnenberg, F. D. Williams, F. Lipparini, F. Egidi, J. Goings, B. Peng, A. Petrone, T. Henderson, D. Ranasinghe, et al. *Gaussian 16, Revision B.01*, Gaussian Inc, Wallingford, CT, USA **2016**.
[48] A. D. Becke, *J. Chem. Phys.* **1993**, *98*, 5648.
[49] P. J. Stephens, F. J. Devlin, C. F. Chabalowski, M. J. Frisch, *J. Phys. Chem.* **1994**, *98*, 11623.
[50] C. Lee, W. Yang, R. G. Parr, *Phys. Rev. B* **1988**, *37*, 785.

[51] B. Mennucci, R. Cammi, *Continuum Solvation Models in Chemical Physics*, John Wiley & Sons Ltd, Chichester, UK **2007**.
[52] B. Mennucci, J. Tomasi, R. Cammi, J. R. Cheeseman, M. J. Frisch, F. J. Devlin, S. Gabriel, P. J. Stephens, *J. Phys. Chem. A* **2002**, *106*, 6102.
[53] M. E. Casida, in *Recent Advances in Density Functional Methods*, Vol. *1* (Ed.: D. P. Chong), World Scientific, Singapore **1995**, Ch. 5.
[54] Y. Zhou, B. Yan, D. Z. Tan, J. J. Zhou, Q. B. Guo, W. Jiang, C. Xu, X. F. Liu, J. R. Qiu, R. S. Liu, X. Y. Chen, *Nanoscale* **2015**, *7*, 4063.
[55] X. Meng, S.-Y. Song, X.-Z. Song, M. Zhu, S.-N. Zhao, L.-L. Wu, H.-J. Zhang, *Inorg. Chem. Front.* **2014**, *1*, 757.
[56] D. Zhao, D. Yue, K. Jiang, L. Zhang, C. Li, G. Qian, *Inorg. Chem.* **2019**, *58*, 2637.